# Electronic Supplementary Information

## Unveiling the mechanism of selective gate-driven diffusion of $CO_2$ over $N_2$ in MFU-4 metal-organic framework.

G. Sastre,[a] J. van den Bergh[b], F. Kapteijn[b], D. Denysenko[c] and D. Volkmer[c]

[a] Instituto de Tecnologia Quimica UPV-CSIC. Universidad Politecnica de Valencia. 46022 Valencia, Spain. E-mail: gsastre@itq.upv.es

[b] Catalysis Engineering, Chemical Engineering Department, Delft University of Technology, Julianalaan 136, 2628 BL Delft, The Netherlands.

[c] Chair of Solid State and Materials Chemistry, Institute of Physics, Augsburg University, Universitaetsstrasse 1, D-86159 Augsburg, Germany. E-mail: dirk.volkmer@physik.uni-augsburg.de

## Contents:

## 1. Energetics of $CO_2$ and $N_2$ in MFU-4

The computational strategy followed in this work consists of two different parts. Here in the first part, a cluster model of MFU-4 has been considered in order to calculate the energies of $CO_2$ and $N_2$ in specific locations near the small pore. This is not a full exploration of the trajectories followed by the sorbates but it will be a first estimation on whether different diffusional behaviours for $CO_2$ and $N_2$ in MFU-4 can be expected.

Gaussian09 software and DFT methods have been used throughout. Several functionals (B3LYP, PBE and CAM-B3LYP) have been tested with CAM-B3LYP chosen due to its capability to account for long-range corrections introduced in the functional through the Coulomb-attenuating method.

Large basis sets are required jointly to the use of long-range correction in order to capture the physics of the dispersion interactions. Due to the large size of the system, we have opted by using the Def2-QZVP basis set only for the diffusing molecule (either $N_2$ or $CO_2$) and also the atoms located in the neighbourhood of the diffusing molecule, which means the 8 Cl atoms as well as those Zn and H atoms located nearby. All the other atoms were kept fixed and were described with 3-21G basis set. Including the diffusing molecule, this gives 1873 basis functions (cluster-MFU-4 + $N_2$) and 1894 basis functions (cluster-MFU-4 + $CO_2$).

Geometry optimisation in this system poses a considerable challenge given the non-bonding nature of the reaction path and also due to the swallowness of the potential energy surface, and hence some of the four default criteria for convergence were relaxed. Convergence is usually tested against threshold values for the maximum force component, root-mean square force, maximum step component, and root-mean-square step, but in some cases resulting energy differences between subsequent steps below $10^{-4}$ Ha were taken as converged if the number of optimisation cycles exceeded 200.

### *Diffusion path of $N_2$.*

Diffusion of $N_2$ through MFU-4 does not contain any unexpected behaviour due to the fact that none of the atoms of the MFU-4 cluster interacts strongly with the diffusing molecule. The diffusion follows a trajectory as that depicted in Figure S1, where the relevant energies obtained are shown.
The transition state is defined by the geometry in which the $N_2$ molecule is located at the middle of a 4Cl-face. At this point is illustrative to consider that the distance between diagonal Cl atoms in the 4Cl-face where $N_2$ is located is 6.3 Å, whilst the equivalent distance in the parallel 4Cl-gate is 5.8 Å. This indicates a certain repulsion between the electronic clouds of the $N_2$ molecule and the neighbour Cl anions but it is not a major interaction. In spite of this repulsion, the $N_2$ molecule is not large enough so as to force a Cl atom out of the plane of the 4Cl-face. The 8Cl-cube can remain ‘close’ while $N_2$ is inside. Overall, this results in a relative energy minimum as shown in geometry ‘3’ (Figures S1 and S2).

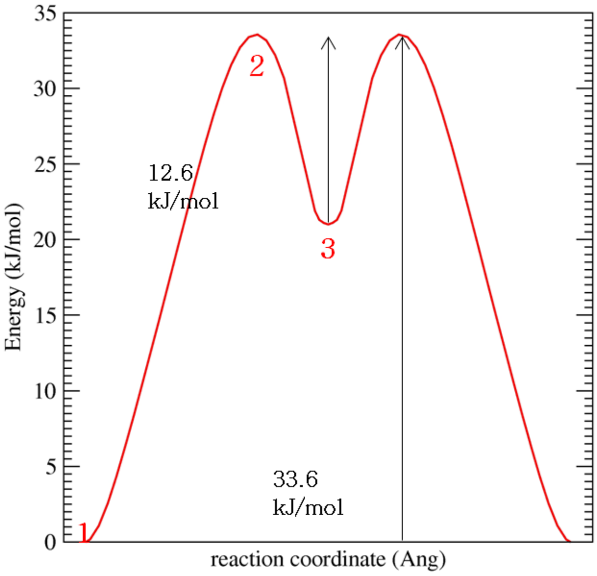

**Figure S1**. Diffusion path of $N_2$ through the small pore of MFU-4 using the cluster indicated in Figure S2. Energies from CAM-B3LYP/Def2-QZVP.

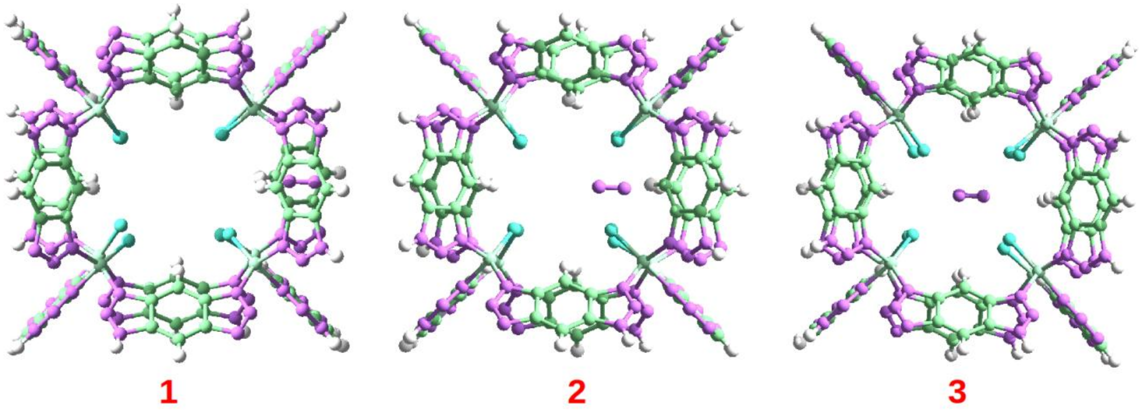

**Figure S2**. Geometries of the diffusion path of $N_2$ through the small pore of MFU-4 corresponding to Figure S1.

*Diffusion path of $CO_2$.*

A different picture was obtained for $CO_2$, in which, additionally to the same diffusion path than that of $N_2$, an alternative diffusion path with a lower activation energy has been found. First, the equivalent diffusion path can also be followed and this involves crossing the $CO_2$ molecule across a 4Cl-face, but this path (2’→3 in Figure S3) presents particular features with respect to the previous case. A minimum (rather than a maximum like in the case of $N_2$) has been found for the geometry corresponding to the molecule located at position '2' (see Figure S3). Two reasons justify that this is a minimum rather than a maximum: (i) the $CO_2$ molecule consists of three atoms rather than two and bears a charge separation between C and O (unlike the N atoms which are neutral), with the C atom having a net positive charge and hence being electrostatically stabilised by the negative charge of the neighbour Cl atoms in the 4Cl-face; (ii) one of the Cl atoms shifts off the 4Cl-face which causes the 8Cl-cube to 'open a gate' (see geometry '2' in Figure S4), with more room available for the incoming molecule.

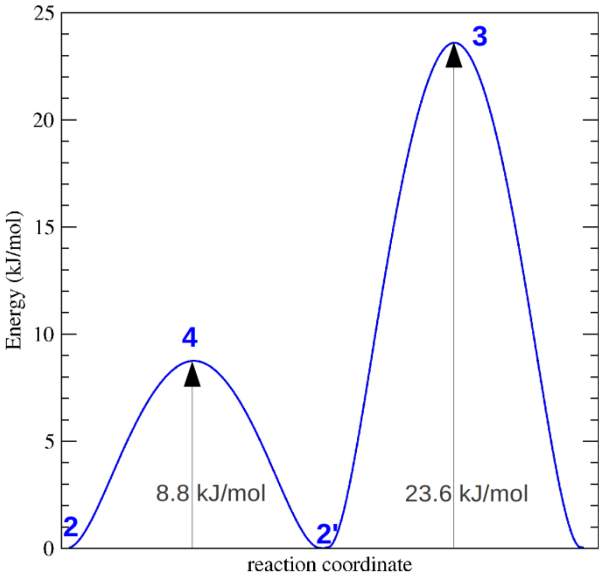

**Figure S3**. Diffusion path of $CO_2$ through the small pore of MFU-4 using the cluster indicated in Figure S4. Energies from CAM-B3LYP/Def2-QZVP.

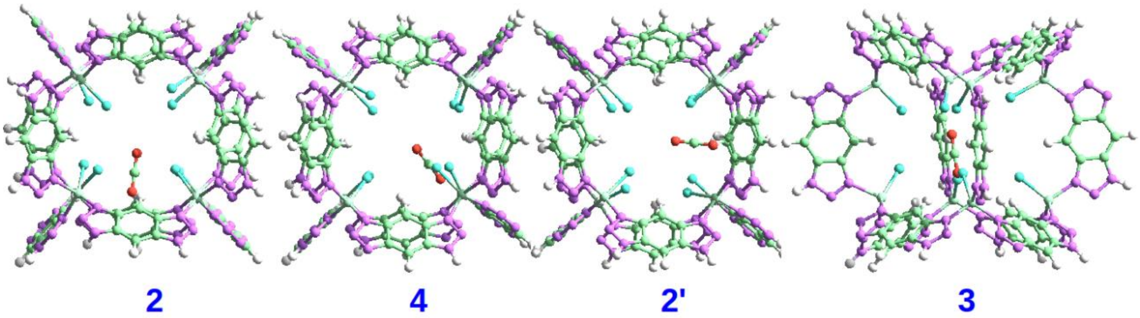

**Figure S4**. Geometries of the diffusion path of $CO_2$ through the small pore of MFU-4 corresponding to Figure S3. ‘Geometry 3’ in this figure has been rotated 90º in the vertical axis in order to appreciate better that the $CO_2$ molecule is at the centre of the 8Cl-cube.

This unfavourable path (2’→3 in Figure S3) indicates that when $CO_2$ is inside the 8Cl-cube, a transition state (rather than a minimum like in the case of $N_2$) is found. The corresponding activation energy is slightly smaller (23.6 kJ/mol) than in the case of $N_2$ (33.6 kJ/mol).

A second (favourable) path for diffusion (2→4 in Figure S3), not present in the case of $N_2$, has been found for $CO_2$. This represents a hopping mechanism between two different 4Cl-faces in the 8Cl-cube, and these two 4Cl-faces are respectively connected to different large cages. Hence, this represents a large→small→large pore migration and it is an overall mechanism for diffusion, with a smaller activation energy (8.8.kJ/mol). Two reasons that explain the low energy of this transition state are: (i) the relatively unhindered rotational motion of the Cl atom due to a floppy angle Cl-Zn-N, and (ii) the additional stabilisation of the $CO_2$ molecule with one hydrogen from a neighbour benzene ring with $CO_2$ becoming coplanar with such benzene ring (Figure S5).

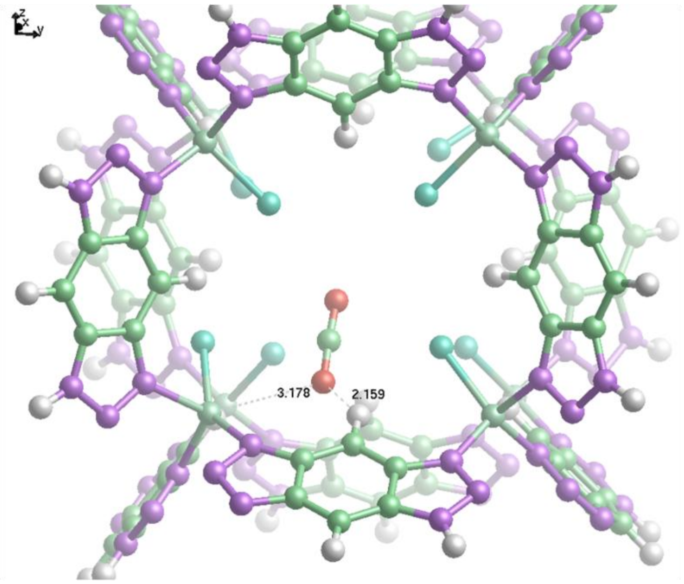

**Figure S5**. Detail of ‘Geometry-4’ (Figure S4) corresponding to the transition state of large→small→large pore hopping. Diffusion path of $CO_2$ through the small pore of MFU-4 as described in Figures S3 and S4.

*Conclusions from energy minimisations.*

As conclusions, these results suggest a faster diffusion of $CO_2$ over $N_2$ in MFU-4, but this energy minimization study does not give any information on how probable would be the respective hopping mechanisms found, nor gives information about: the time of residence of each molecule in the small pore, the effects of loading and temperature. For these reasons, in the second part of this computational strategy, below, a new force field has been parameterized in order to perform a dynamic study.

## 2. Details of the parameterisation of a force field for MFU-4|$CO_2$|$N_2$

Figures S6 and S7 show van der Waals interactions Cl-Cl and H-H from several Lennard-Jones terms found in the literature.

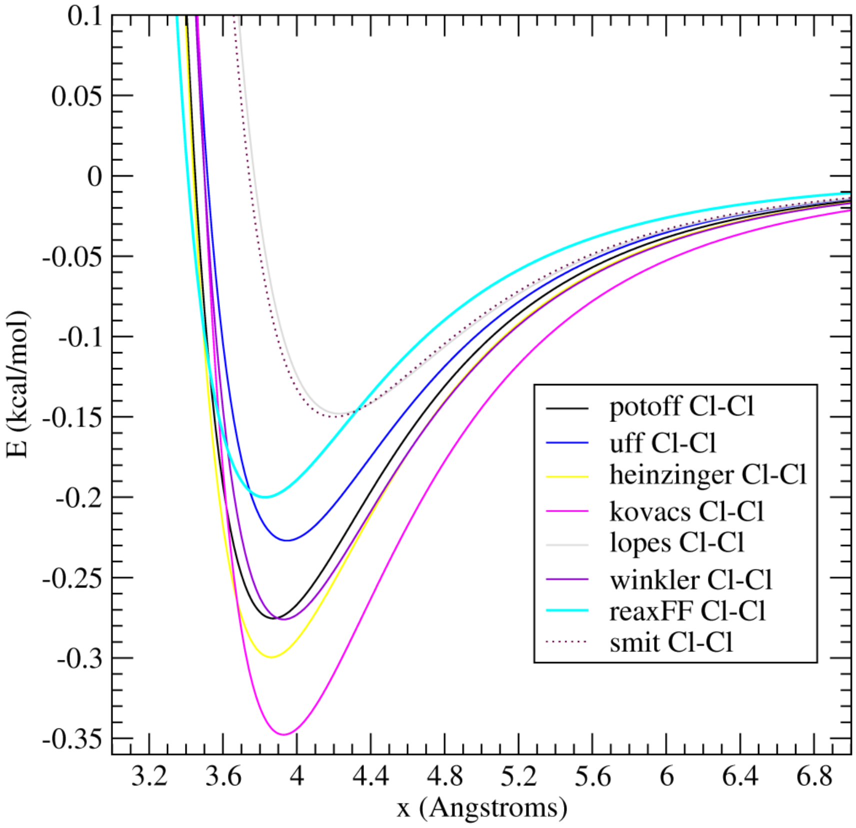

**Figure S6**. Energies corresponding to the Cl—Cl van der Waals interactions using the referred force fields. Potoff[1], UFF[2], Heinzinger[3], Kovacs[4], Lopes[5], Winkler[6], reaxFF[7], Smit[8].

In the present procedure, we have used combinations of the epsilon and sigma Lennard-Jones parameters corresponding to the force fields plotted in Figures S6 and S7 as well as a new parameter for the Cl-Zn-N bending in order to reproduce as accurately as

---

[1] G. Kamath, G. Georgiev and J. J. Potoff; "Molecular Modeling of Phase Behavior and Microstructure of Acetone-Chloroform-Methanol Binary Mixtures"; *J. Phys. Chem. B* 2005, ***109***, 19463-19473.

[2] A. K. Rappe, C. J. Casewit, K. S. Colwell, W. A. Goddard and W. M. Skiff, *J. Am. Chem. Soc.* 1992, **114**, 10593.

[3] (a) W. Dietz and K. Heinzinger; Ber. Bunsenges. Phys. Chem. 1984, 8, 543. (b) Dietz and Heinzinger force field cited in: I. G. Tironi and W. F. van Gunsteren; "A molecular dynamics simulation study of chloroform"; Mol. Phys. 1994, **83**, 381-403.

[4] H. Kovacs, J. Kowalewski and A. Laaksonen; J. Phys. Chem. 1990, **94**, 7378.

[5] J. N. Canongia-Lopes, J. Deschamps and A. A. H. Padua; "Modeling Ionic Liquids Using a Systematic All-Atom Force Field"; J. Phys. Chem. B 2004, **108**, 2038-2047.

[6] J. Harnes, M. Abu-samha, H. Bergersen, M. Winkler, A. Lindblad, L. J. Sæthre, O. Björneholm and K. J. Børve; "The structure of mixed methanol/chloroform clusters from core-level photoelectron spectroscopy and modeling."; *New J. Chem.* 2011, **35**, 2564-2572.

[7] O. Rahaman, A. C. T. van Duin, S. Vyacheslav, S. Bryantsev, J. E. Mueller, S. D. Solares, W. A. Goddard III and J. Douglas; "Development of a ReaxFF Reactive Force Field for Aqueous Chloride and Copper Chloride"; *J. Phys. Chem. A* 2010, ***114***, 3556–3568.

[8] Z. Liu, T. Chen, A. Bell and B. Smit; "Improved United-Atom Force Field for 1-Alkyl-3-methyl-imidazolium Chloride"; *J. Phys. Chem. B* 2010, ***114***, 4572–4582.

possible, with the new-FF, the DFT energies of the configurations explored. With the new-FF parameters (Table S1), the comparison of the new-FF and DFT energies indicates an improved performance with respect to the UFF results.

This procedure, using DFT data obtained with the ωB97XD functional, was also carried out using other dispersion-corrected functional such as: B97-D3, M06X-D3, CAM-B3LYP-D3, and B2PLYP-D. From an overall comparison of results, the functional ωB97XD was selected.

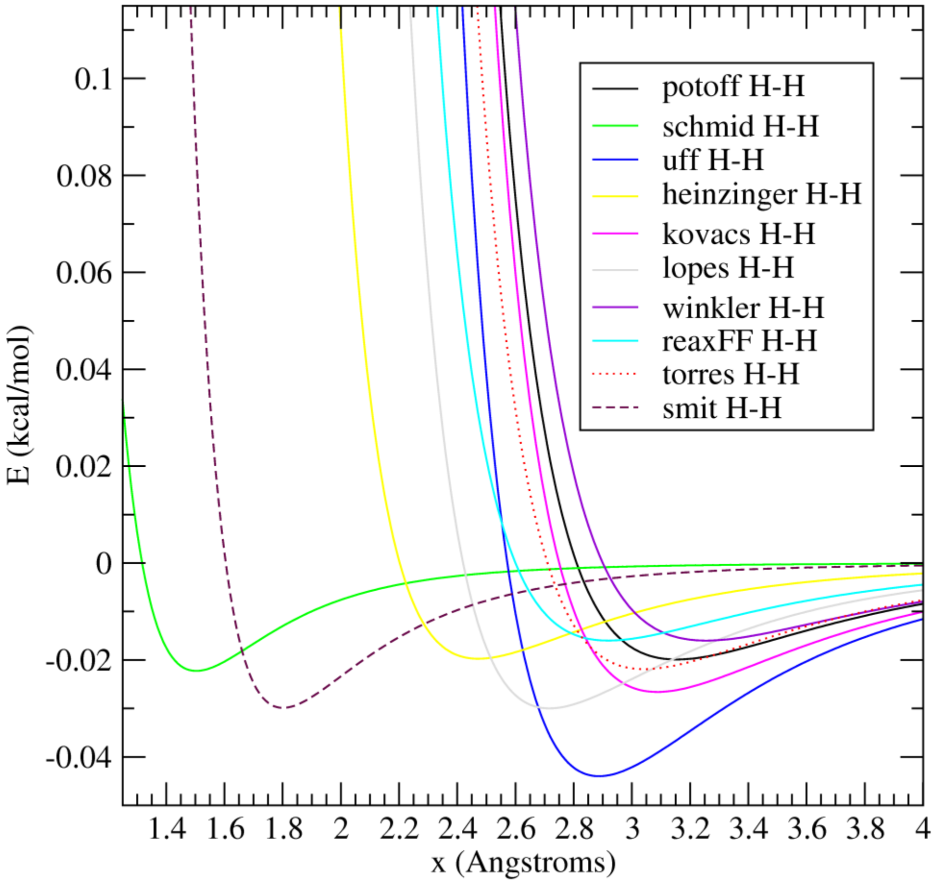

**Figure S7**. Energies corresponding to the H—H van der Waals interactions using the referred force fields. Potoff[1], Schmid[9], UFF[2], Heinzinger[3], Kovacs[4], Lopes[5], Winkler[6], ReaxFF[7], Torres[10], Smit[8].

**Table S1**. Parameters that have been changed from UFF to simulate MFU-4 (equations 1 and 2).

| | $\varepsilon_{Cl}$ (kcal/mol) | $\sigma_{Cl}$ (Å) | $\varepsilon_{H}$ (kcal/mol) | $\sigma_{H}$ (Å) | $k_{Cl\text{-}Zn\text{-}N}$ (kcal/mol) |
|---|---|---|---|---|---|
| **new-FF** | 0.200 | 3.828 | 0.023 | 1.482 | 18.5 |
| **UFF** | 0.227 | 3.947 | 0.044 | 2.886 | 141.4 |

---

[9] S. Bureekaew, S. Amirjalayer, M. Tafipolsky, C. Spickermann, T. K. Roy and R. Schmid, “MOF-FF A flexible first-principles derived force field for metal-organic frameworks”, *Phys. Status Solidi B* 2013, 1.

[10] E. Torres, G. A. DiLabio, “Density-Functional Theory with Dispersion-Correcting Potentials for Methane: Bridging the Efficiency and Accuracy Gap between High-Level Wave Function and Classical Molecular Mechanics Methods”, *J. Chem. Theory Comput.* 2013, **9**, 3342-3349.

The interaction energy between each sorbate molecule and the MFU-4 cluster has been calculated at the ωB97XD/TZVP level. Using the condition that the new-FF energy obtained should be as close as possible to the DFT value, and with the atomic charges in the new-FF obtained from the Mulliken analysis of the DFT results, the following parameters were obtained.

**Table S2**. Parameters that have been changed from UFF to simulate the interaction of MFU-4 with $CO_2$ and $N_2$ (equation 1). C1 is carbon in $CO_2$, O1 is oxygen in $CO_2$, N1 is nitrogen in $N_2$

| | $\varepsilon_{C1}$ (kcal/mol) | $\sigma_{C1}$ (Å) | $\varepsilon_{O1}$ (kcal/mol) | $\sigma_{O1}$ (Å) | $\varepsilon_{N1}$ (kcal/mol) | $\sigma_{N1}$ (Å) |
|---|---|---|---|---|---|---|
| **new-FF** | 0.161 | 3.420 | 0.055 | 3.897 | 0.059 | 3.860 |
| **UFF** | 0.105 | 3.851 | 0.060 | 3.500 | 0.069 | 3.660 |

**Table S3**. Atomic charges used in the new-FF. C6 is carbon in benzene ring (MFU-4), C1 is carbon in $CO_2$, N3 is nitrogen in pyrazolate ring (MFU-4), N1 is nitrogen in $N_2$, O1 is oxygen in $CO_2$. $Zn_o$ and $Zn_t$ are octahedral and tetrahedral Zn in MFU-4, H is hydrogen in MFU-4 and Cl is chlorine in MFU-4.

| q(C6)$^{(1)}$ | q(C1) | q(N3)$^{(2)}$ | q(N1) | q(O1) | q($Zn_o$) | q($Zn_t$) | q(H) | q(Cl) |
|---|---|---|---|---|---|---|---|---|
| -0.080<br>-0.158 | 0.550 | 0.021<br>-0.075 | 0.000 | -0.275 | 0.862 | 0.710 | 0.150 | -0.480 |

(1); -0.080 and -0.158 for carbons without and with C-H bonds respectively

(2); 0.021 and -0.075 for central and lateral N in N-N-N pyrazolate respectively.

Using the new-FF, some geometry optimisations have been performed and the results have been compared with ωB97XD/TZVP calculations. Both methods, the ωB97XD/TZVP and the new-FF optimisations, find interesting minimum energy conformations of $CO_2$ interacting with MFU-4 (Figure S8). This is also observed in the subsequent molecular dynamics and it contributes to open the 8Cl-gate and leave more space for $CO_2$ to penetrate into the small 8Cl-cube.

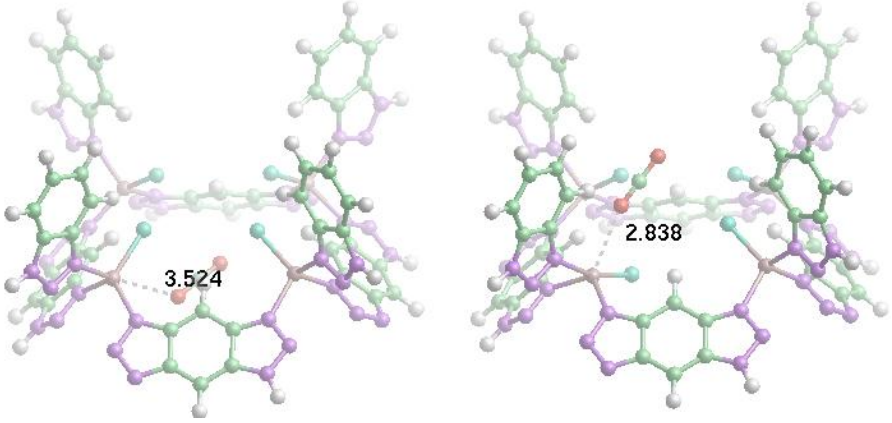

**Figure S8**. Two relative minima of $CO_2$ interacting with the MFU-4 cluster, found with both methods, ωB97XD/TZVP and the new-FF. (left) The geometry shows the absolute minimum. (right) The geometry shows a rotated Cl ligand. Zn shows in both cases a trigonal bipyramid coordination. The conformation at right contributes to open the gate of the small pore in MFU-4. Highlighted distances in Å.

## 3. Molecular dynamics of $CO_2$ and $N_2$ diffusing in MFU-4

With the new-FF, several molecular dynamics runs of 2 ns were performed using the LAMMPS software. The NVT ensemble was employed using the experimental unit cell parameters of MFU-4 ($a$ = 21.697 Å). The time step selected was 0.1 fs. The sequence of calculations in each run was: 500 steps of energy minimisation at 0 K starting from the initial configuration; 10000 equilibration steps of molecular dynamics at each of the following temperatures: 98, 198, and 298 K; and then the final 2 ns run (20 million steps) at the target temperature from which all the subsequent analysis was performed. Five molecular dynamics runs were studied in detail. Movies 1-3 have been added as further electronic supplementary information. Movies 4 and 5, as well as extended versions of the movies 1-3 are not included as supplementary information but are available from the authors upon request.

### 1. Low loading of $CO_2$ at 298 K (movie 1).

10 molecules of $CO_2$ were located in the unit cell of MFU-4. In spite of the large mobility of the Cl atoms in the small cage of MFU-4, no events showing diffusion through the small pore have been found. The same happens with this loading of $N_2$ molecules. The molecules tend to locate relatively far from the 4Cl-gates of the 8Cl-cube.

### 2. High loading of $CO_2$ at 298 K (movie 2).

20 molecules of $CO_2$ were located in the unit cell of MFU-4. A large number of small pore crossing events have been observed. With this higher loading, some molecules locate closer to the 4Cl-gates than in the previous case and this larger pressure contributes to the higher diffusivity.

A plot of the $x,y,z$ coordinates versus time of simulation, where only the $CO_2$ molecules crossing the small pore have been selected (Figure S9), allows to appreciate each of the diffusion events. One of the figures (Figure S9, right) shows all 20 $CO_2$ molecules.

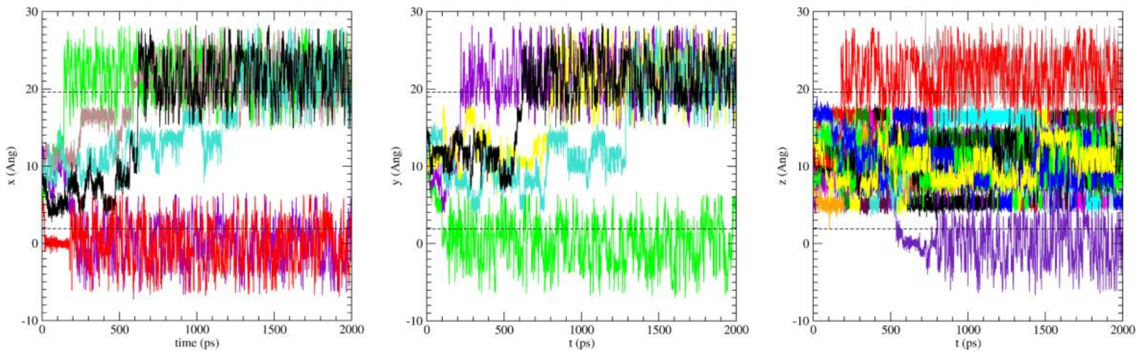

**Figure S9**. $x,y,z$ (left, middle,right) coordinates versus simulation time. Boundaries of the large pore (where initially all 20 $CO_2$ molecules are located) are indicated with a dashed line. Diffusion appears each time such lines are crossed. 11 crossing events are found, most of which (9) belong to a large→small→large pore hopping event.

Very importantly, Figure S9 shows that nine (out of eleven) crossing events are of the type large→small→large pore, which means that $CO_2$ does not remain in the small cage for long. The reason for that is that $CO_2$ is long enough so as to keep (at least) one of the Cl-gates open, and hence hopping out becomes easier. This contributes to increase diffusivity.

### 3. High loading of $N_2$ at 298 K (movie 3).

20 molecules of $N_2$ were located in the unit cell of MFU-4. Contrary to what happens with $CO_2$, $N_2$ does not diffuse much. One of the reasons can be the slightly higher activation energy as found from the comparison of Figures S1-S4. Figure S10 allows to appreciate less crossing events than in the previous case. But also another difference appears.

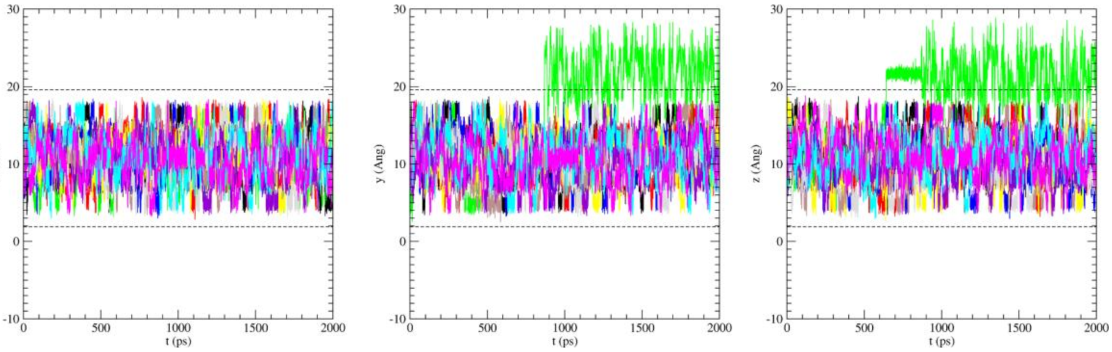

**Figure S10**. *x*,*y*,*z* (left, middle,right) coordinates versus simulation time. Boundaries of the large pore (initial location of the 20 $N_2$ molecules) are indicated with a dashed line. Diffusion appears each time such lines are crossed. Only 2 crossing events are found, one of which (middle) belongs to a large→small→large pore hopping event, whilst the other (right) occurs with a long residence time (650-850 ps) in the small pore, as indicated by the narrow oscillation of the '*z*' coordinate.

The main difference here is that the $N_2$ molecule can not escape from the small 8Cl-cube cage so easily. In Figure S10 (right), it is shown a ca. 200 ps elapsed time (from 650 to 850 ps) in which a $N_2$ molecule remains occluded in the small pore. Figure 9 (main manuscript) shows that with $N_2$ inside, the small pore can remain in the closed gate conformation.

### 4. High loading of $CO_2$ at 298 K using UFF instead of new-FF (movie 4).

20 molecules of $CO_2$ were located in the unit cell of MFU-4. The movies show a much slower mobility for the $CO_2$ molecules and in fact no diffusion is observed. Some of the reasons are the incorrect energetics of the intermolecular sorbate|MFU-4 interactions, and also the wrong behaviour of the mobility of the Cl atoms in the small cage due to a very large force constant for the Cl-Zn-N bond angle term.

5. High loading of $CO_2$ at 348 K (movie 5).

20 molecules of $CO_2$ were located in the unit cell of MFU-4. At this larger temperature, a very similar picture to that of 298 K appears, with a similar number of crossing events. On the one hand it is clear that the kinetic energy of the sorbate molecules should contribute to a larger diffusivity, but somehow this effect is not dominant. A more important effect is observed from pressure than from temperature. In any case, a careful study of diffusivity dependence with temperature has not been performed and this is left for future work.

## 4. Isosteric heats of adsorption for $CO_2$ and $N_2$ in MFU-4 and MFU-4*l*(arge)

Two very similar MOFs, MFU-4 and MFU-4l(arge), have been used for the following adsorption experiments. The only difference between the two structures is the organic linker, which in the case of MFU-4l(arge) is larger[11].

The difference between isosteric heats of $CO_2$ and $N_2$ adsorption at zero loading (24.4 and 14.7 kJ $mol^{-1}$, respectively) for MFU-4 is 9.7 kJ $mol^{-1}$ and matches very well the difference between calculated values (18.0 and 9.6 kJ $mol^{-1}$, respectively). Interestingly, for MFU-4*l*, with larger pores, the difference between $CO_2$ and $N_2$ adsorption heats at zero loading is much lower (16.8 and 13.2 kJ $mol^{-1}$, respectively). This shows that probably considerable interaction between $CO_2$ molecules and tetrahedrally coordinated $Zn^{2+}$ centers takes place in MFU-4 case, but is much less pronounced for MFU-4*l*. The dependences of isosteric heats of adsorption on loading are shown in Figures 5 and S13.

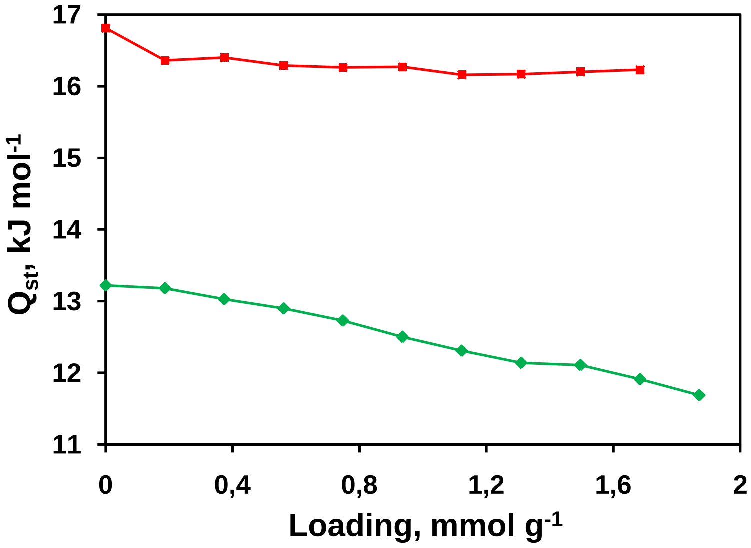

**Figure S13.** Dependences of the isosteric heats of adsorption on loading for $CO_2$ (red) and $N_2$ (green) in MFU-4*l*.

The sample of MFU-4 was degassed for 20 h at 320 °C before the first measurement and for 2 h at 150 °C between the measurements under high vacuum ($P < 10^{-4}$ mbar). The sample of MFU-4*l* was degassed for 20 h at 200 °C before the first measurement

---

[11] D. Denysenko, M. Grzywa, M. Tonigold, B. Streppel, I. Krkljus, M. Hirscher, E. Mugnaioli, U. Kolb, J. Hanss, D. Volkmer, *Chem. Eur. J.* 2011, **17**, 1837.

and for 2 h at 150 °C between the measurements under high vacuum ($P < 10^{-4}$ mbar). Adsorption isotherms were measured with a BELSORP-max instrument combined with a BELCryo system. For the determination of isosteric heats of adsorption for MFU-4, four isotherms at 283, 293, 303 and 313 K for $CO_2$ and five isotherms at 183, 193, 194.7, 203 and 213 K for $N_2$ were measured (Figures S14-S15). The equilibration of $N_2$ adsorption isotherms has been proven by repeating the measurement at lowest temperature (183 K) with longer equilibration time, whereas the same result was obtained using two different equilibration criteria, as shown in Figure S16 (criterion 1 – pressure change < 0.3 % within 500 s, criterion 2 – pressure change < 0.3 % within 750 s). Equilibrium criterion 1 was used for all other isotherms. For the determination of isosteric heats of adsorption for MFU-4*l*, four isotherms at 243, 253, 263 and 273 K for $CO_2$ and 163, 173, 183 and 193 K for $N_2$ were measured (Figures S17-S18). The isosteric heats of adsorption were calculated from the measured isotherms using the Clausius-Clapeyron equation (**I**). The slopes of linear plots ln$P$ versus $1/RT$ for different loadings (Figures S19-S22) give the adsorption enthalpies, according to the equation (**II**).

$$Q_{st} = -R\left(\frac{\partial(\ln P)}{\partial(1/T)}\right)_{\theta}$$ (**I**), $\theta$ – surface coverage

$$\ln P = -\frac{Q_{st}}{R}\left(\frac{1}{T}\right) + C$$ (**II**), C – integration constant

The isosteric heats of adsorption at zero limit surface coverage (initial heat of adsorption) have been determined using Henry's constants $K_H$, obtained as a slope from the linear ranges of isotherms at low pressure (Tables S6-S9 and Figures S23-S26). In this range the dependence of amount adsorbed ($n$) on the pressure can be expressed with Henry's law (**III**). The initial isosteric heat of adsorption can be obtained in a similar way by using the Clausius-Clapeyron equation (**IV**) (Figures S27-S28).

$$n = K_H \bullet P$$ (**III**)

$$\lim_{n\to 0}(Q_{st}) = Q_{st}^{0} = R\left(\frac{\partial(\ln K_H)}{\partial(1/T)}\right)$$ (**IV**)

**Table S6.** Henry's constants for $CO_2$ adsorption on MFU-4, $cm^3\ g^{-1}\ kPa^{-1}$

| *T* / K | 283 | 293 | 303 | 313 |
|---|---|---|---|---|
| $K_H$ | 1.591 | 1.1277 | 0.7956 | 0.5918 |

**Table S7.** Henry's constants for $N_2$ adsorption on MFU-4, $cm^3\ g^{-1}\ kPa^{-1}$

| *T* / K | 183 | 193 | 194.7 | 203 | 213 |
|---|---|---|---|---|---|
| $K_H$ | 2.5854 | 1.5828 | 1.4395 | 1.0001 | 0.6669 |

**Table S8.** Henry's constants for $CO_2$ adsorption on MFU-4*l*, $cm^3\ g^{-1}\ kPa^{-1}$

| *T* / K | 243 | 253 | 263 | 273 |
|---|---|---|---|---|
| $K_H$ | 1.1076 | 0.8044 | 0.5901 | 0.4446 |

**Table S9.** Henry's constants for $N_2$ adsorption on MFU-4*l*, $cm^3\ g^{-1}\ kPa^{-1}$

| *T* / K | 163 | 173 | 183 | 193 |
|---|---|---|---|---|
| $K_H$ | 2.6516 | 1.5036 | 0.9174 | 0.5806 |

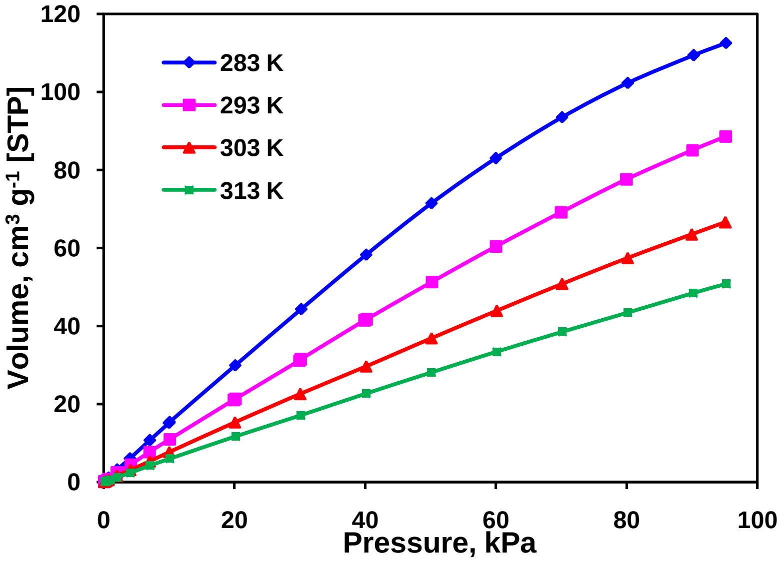

**Figure S14.** $CO_2$ adsorption isotherms for MFU-4.

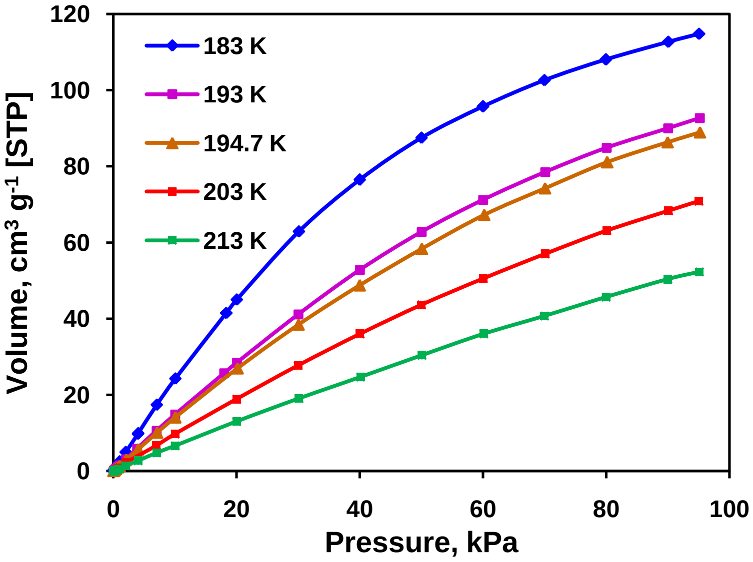

**Figure S15.** $N_2$ adsorption isotherms for MFU-4.

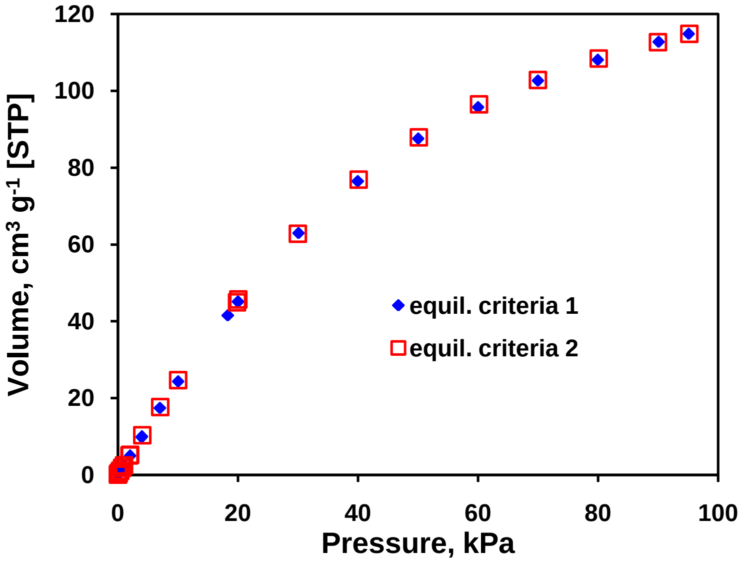

**Figure S16.** $N_2$ adsorption isotherms for MFU-4 at 183 K taken with different equilibration criteria.

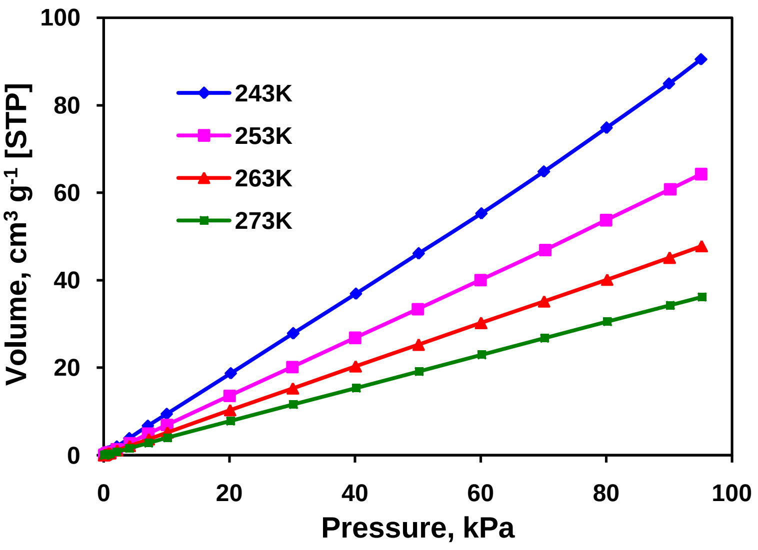

**Figure S17.** $CO_2$ adsorption isotherms for MFU-4*l*.

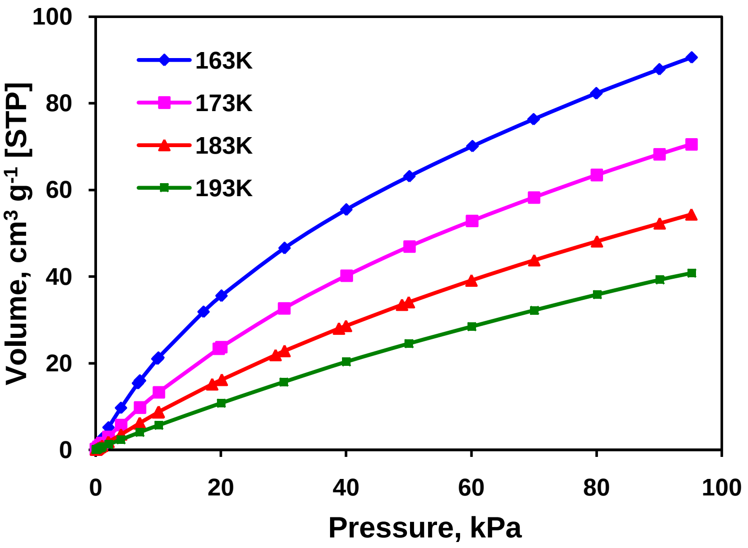

**Figure S18.** $N_2$ adsorption isotherms for MFU-4*l*.

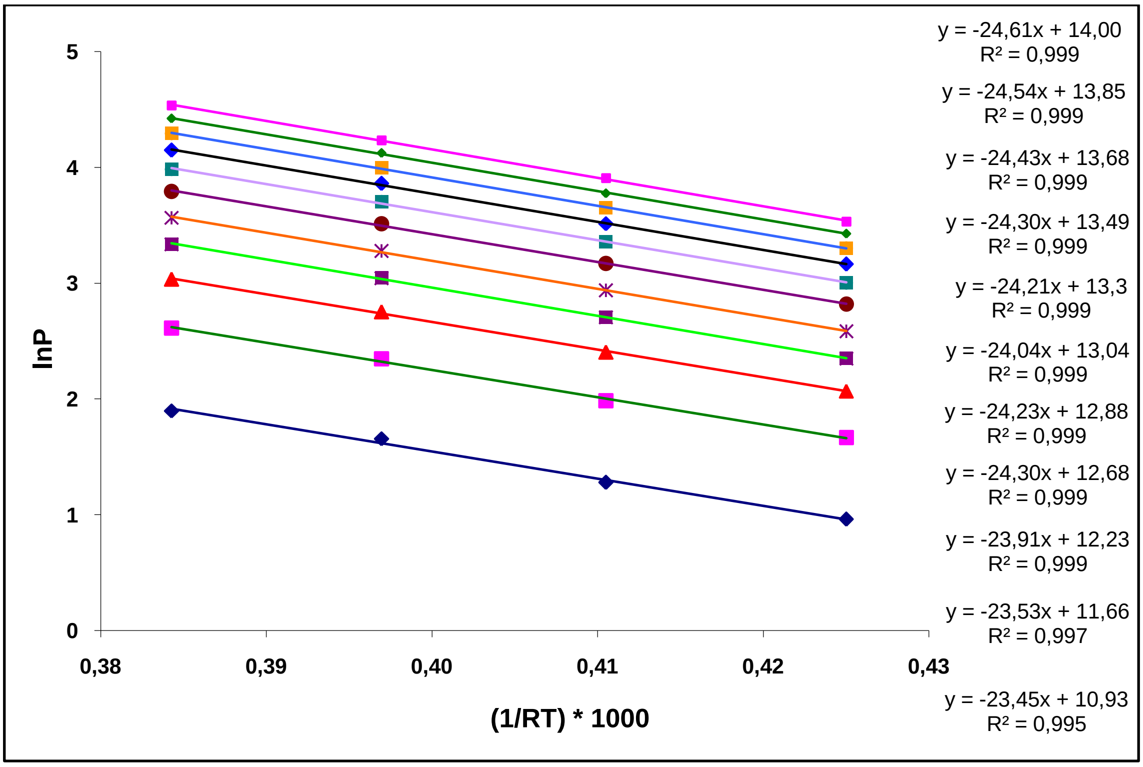

**Figure S19.** ln*P* versus 1/*RT* plots for different loadings for $CO_2$ adsorption in MFU-4.

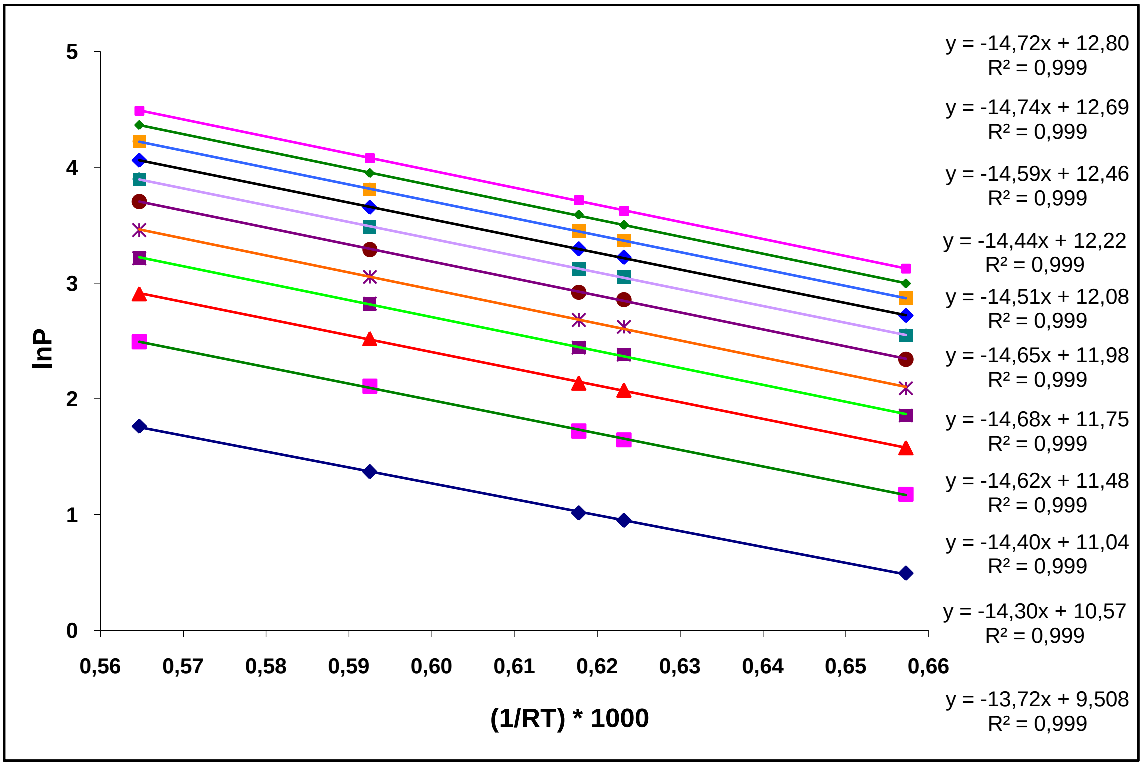

**Figure S20.** ln*P* versus 1/*RT* plots for different loadings for $N_2$ adsorption in MFU-4.

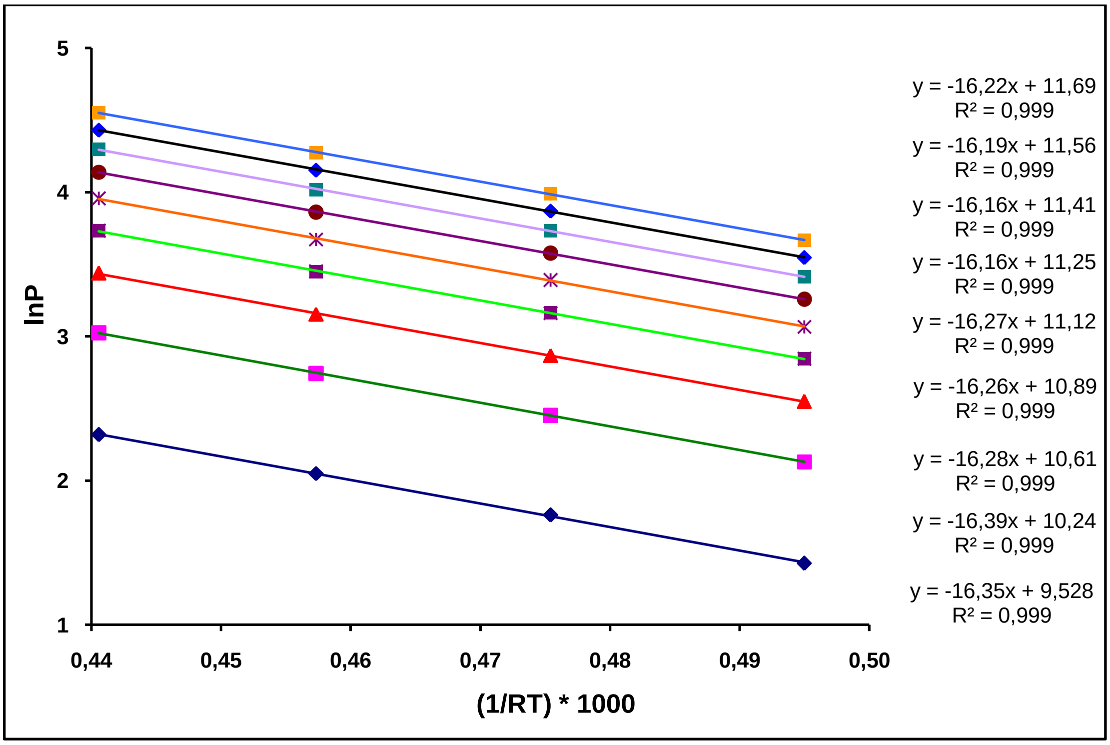

**Figure S21.** ln*P* versus 1/*RT* plots for different loadings for $CO_2$ adsorption in MFU-4*l*.

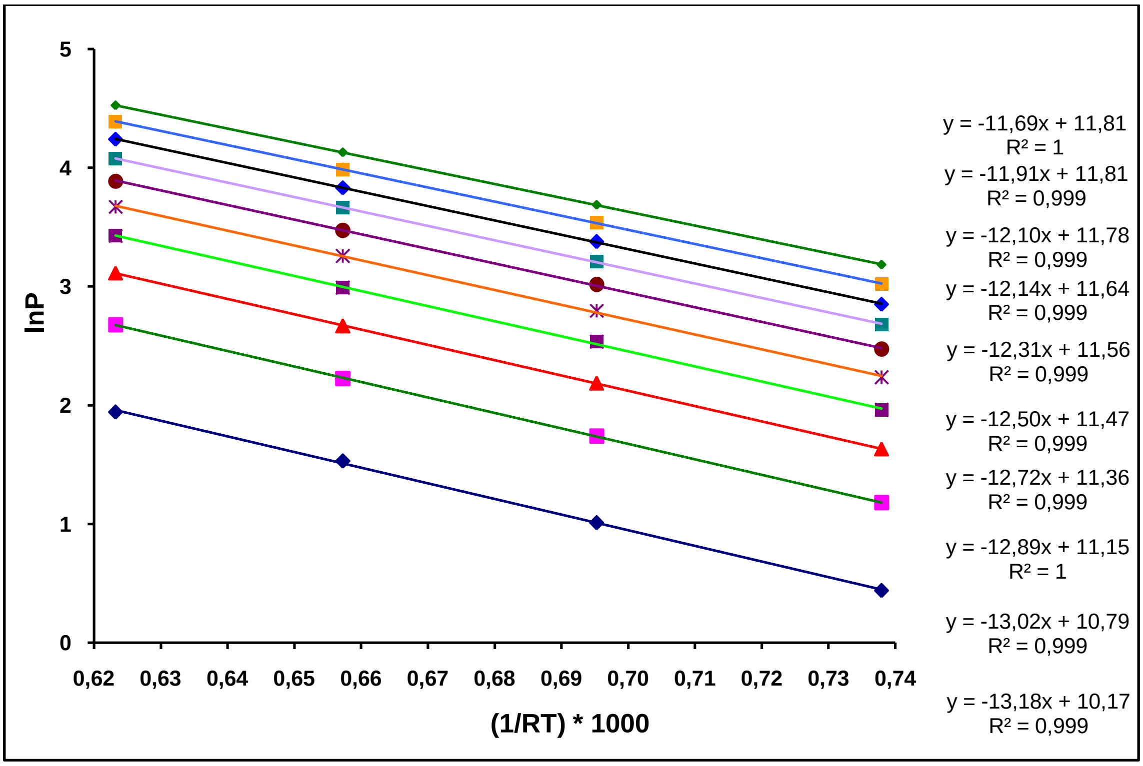

**Figure S22.** ln*P* versus 1/*RT* plots for different loadings for $N_2$ adsorption in MFU-4*l*.

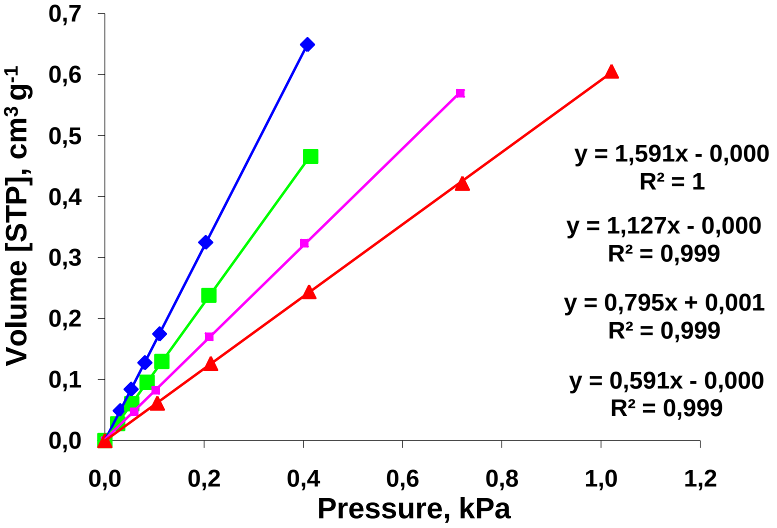

**Figure S23.** Determination of Henry's constants for $CO_2$ adsorption in MFU-4.

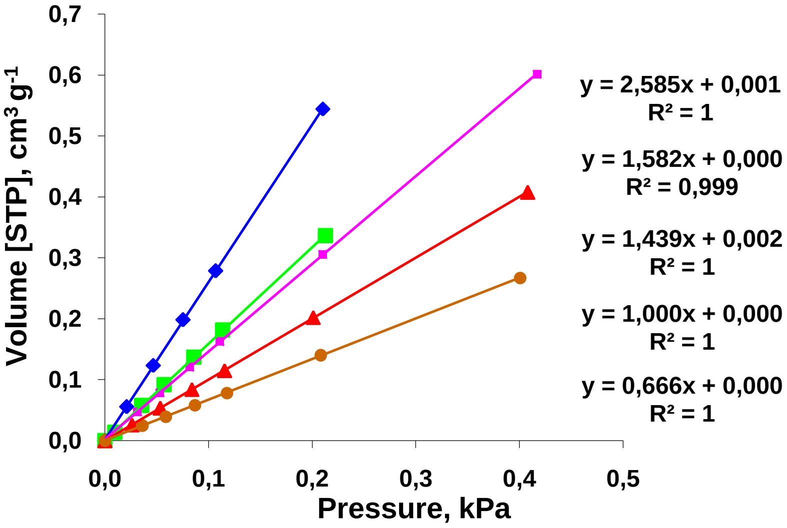

**Figure S24.** Determination of Henry's constants for $N_2$ adsorption in MFU-4.

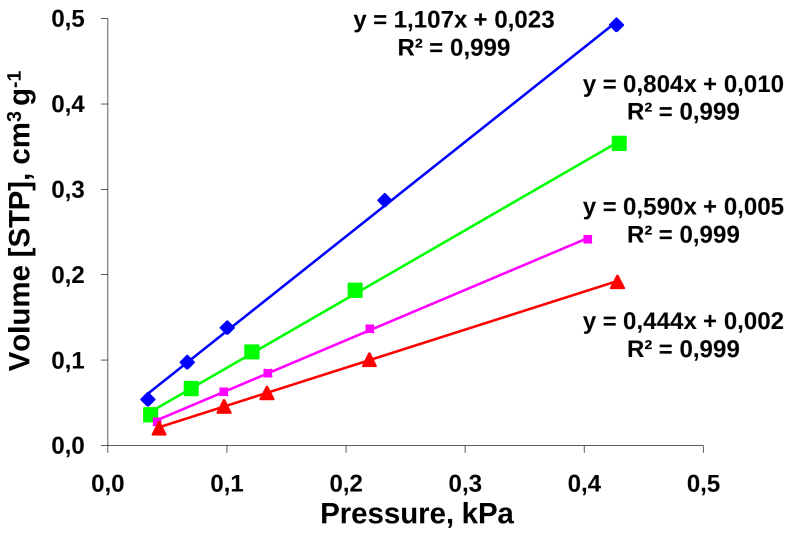

**Figure S25.** Determination of Henry's constants for $CO_2$ adsorption in MFU-4*l*.

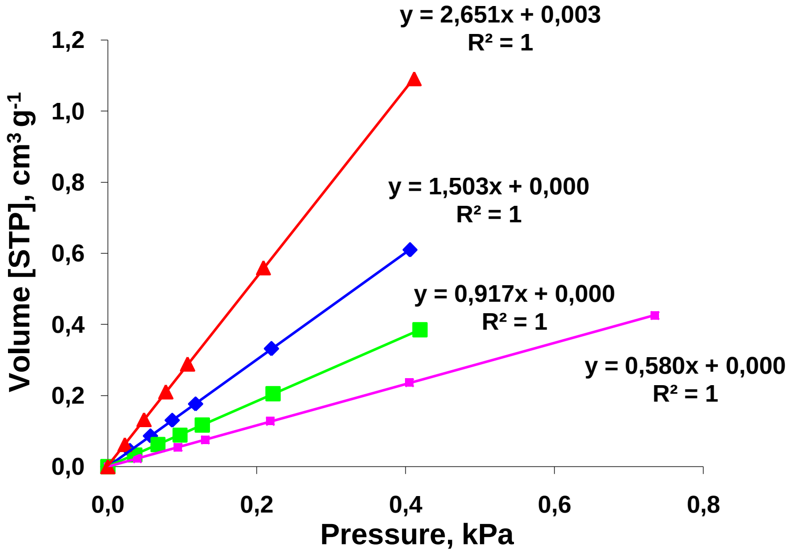

**Figure S26.** Determination of Henry's constants for $N_2$ adsorption in MFU-4*l*.

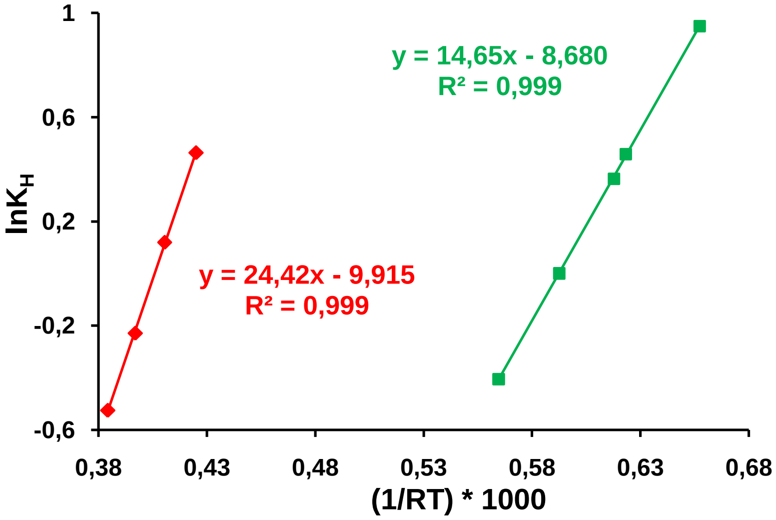

**Figure S27.** ln$K_H$ versus 1/*RT* plots for $CO_2$ (red) and $N_2$ (green) adsorption in MFU-4.

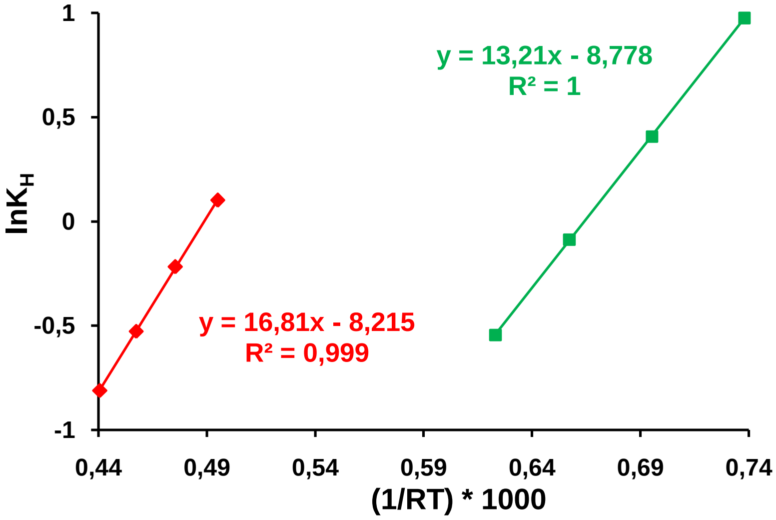

**Figure S28.** ln$K_H$ versus 1/*RT* plots for $CO_2$ (red) and $N_2$ (green) adsorption in MFU-4*l*.

## 5. Determination of diffusivity from uptake measurements

$CO_2$ and $N_2$ equilibrium isotherms and adsorption kinetics have been measured using a Micromeritics ASAP 2010 gas adsorption analyzer (stainless steel version). The instrument was equipped with a turbo molecular vacuum pump and three different pressure transducers (0.13, 1.33, and 133 kPa, respectively) to enhance the sensitivity in different pressure ranges. The static–volumetric technique was used to determine the volume of the gas adsorbed at different partial pressures. In order to optimize the adsorption kinetic measurements the filter that separates the ASAP manifold and sample tube is removed in this case. Since the uptake is calculated based on the pressure at the manifold, this filter could impose mass transport limitations that hamper accurate measurement of the adsorption/desorption kinetics.

The MFU stability was confirmed by recording repetitive $H_2$ isotherms with intermediate thermal treatments. It was found that after the second overnight treatment under vacuum at 423 °C a reproducible isotherm could be obtained. During the series of experiments the samples were treated each night at 423 K under vacuum to ensure comparable sample conditions in all experiments.

Before the adsorbate was contacted with the sample in the uptake measurements, the sample was exposed to 101 kPa of He to obtain thermal equilibrium between the sample and the cooling bath and to determine the free space at the experimental conditions. Then, the sample space was evacuated for 1 h. The uptake curves have been recorded starting from a manifold pressure of 101 kPa and a sample pressure of 0 kPa. The pressure after the uptake was between 70 and 90 kPa, depending on the amount adsorbed. The amount adsorbed was calculated from the measured free space and sample mass (0.178 g).

Information about the apparent diffusivities of $CO_2$ and $N_2$ at 195 and 298 K in MFU4 are obtained by uptake experiments using an ASAP 2000. Upon a pressure step change the slow pressure decay was translated into an uptake profile. The time dependent evolution was interpreted using Fick’s second law with the following assumptions:

- Constant diffusivity, loading independent
- Fick’s law applies
- Uniform particle size or distribution of sizes
- Spherical geometry (cubical structure, 3D pore system)
- Isothermal conditions

$$\frac{\partial q}{\partial t} = D_{app}\nabla^2 q \quad (sphere)$$

$$\frac{\partial \theta}{\partial\left(\frac{t}{t_{90}}\right)} = \left(\frac{t_{90}}{\tau_{diff}}\right)\nabla^2\theta$$

$$\tau_{diff} = \frac{L^2}{D_{app}}$$

$$L = \frac{V}{A}$$

For the model description, uptake profiles (Figure 4) have been normalized for loading $q_{eq}$ (after long equilibration time) and for the time to reach approximately 90% of the loading ($t_{90}$) . This stabilizes the numerical modelling. Further a characteristic diffusion length $L$ is introduced and a characteristic diffusion time $\tau_{diff}$. $t_{90}$ and $q_{max}$ in Figure S29 are 90 and 4700 s (at 298 K and 195 K respectively) and 0.22 and 2.8 mol/kg (at 298 K and 195 K respectively). $t_{90}$ and $q_{max}$ in Figure S30 are 15 and 66 s (at 298 K and 195 K respectively) and 2.2 and 8.0 mol/kg (at 298 K and 195 K respectively).

The partial differential equations have been solved using Athena Visual Studio (www.athenavisual.com) with the following initial and boundary conditions:

$$\begin{array}{lll} t = 0 & \theta = 0 & \forall x \\ t > 0 & \theta = 1 & x = 3 \\ & \dfrac{\partial \theta}{\partial x} = 0 & x = 0 \end{array}$$

At the different time steps the concentration profiles inside the particles have been used to calculate the total amount adsorbed by integration over the particle.

The calculated profile has been compared with those of the $CO_2$ and of $N_2$, both at 195 K and 298 K.

The two nitrogen profiles coincide nicely for the two temperatures, indicating similar diffusion behaviour (Figure S29). For $CO_2$ this correspondence is somewhat less. The 298 K profile shows a fast uptake followed by a somewhat slower evolution to the final state (Figure S30). This one is the most deviating.

The modelled profile using a single particle size does not capture the experimental ones, but gives an indication of the characteristic diffusion times. Slab geometry deviates strongly. Cubic structures are better represented by a spherical geometry. The stronger curvature is not grasped for a single size model, which is attributed to the particle size distribution.

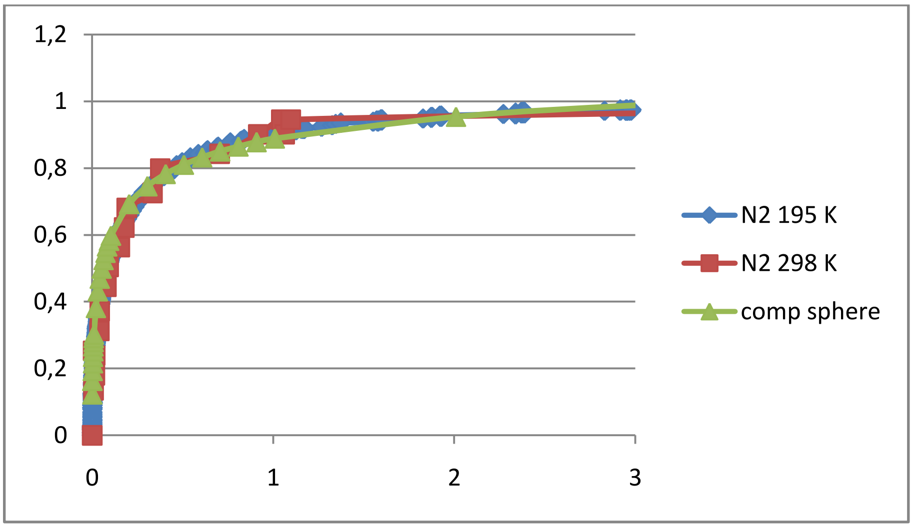

**Figure S29.** Normalized uptake data for $N_2$ at two temperatures and comparison with a composite uptake profile from different particles sizes (spherical geometry).

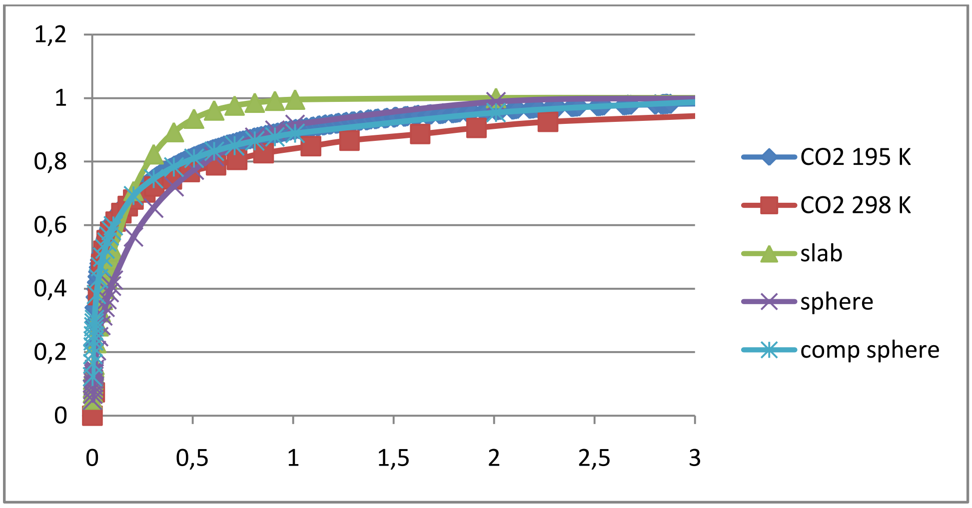

**Figure S30**. Normalized uptake data for $CO_2$ at two temperatures and comparison with single particle size model of slab and sphere and with a composite uptake profile from different particles sizes (spherical geometry).

Contributions of different particle sizes (Figure S31) cover much better this uptake behaviour, and this has been applied here. From the SEM pictures (Figure S32), the cubical particle sizes range globally from 0.5 to 20 micrometer, so the characteristic diffusivity times vary by a factor of ~1000. Seven uptake profiles differing in diffusion time steps of $10^{0.5}$ (logarithmic scale) were used to form the composite uptake profiles (Figures S29 and S30)[12].

---

[12] J. C. Groen, W. Zhu, S Brouwer, K. Ichioka, F. Kapteijn, J. A. Moulijn, and J. Pérez-Ramírez. “Direct demonstration of enhanced diffusion in mesoporous ZSM-5 zeolite obtained via controlled desilication”. *J. Am. Chem. Soc* 2007, **129(2)**, 355-360.

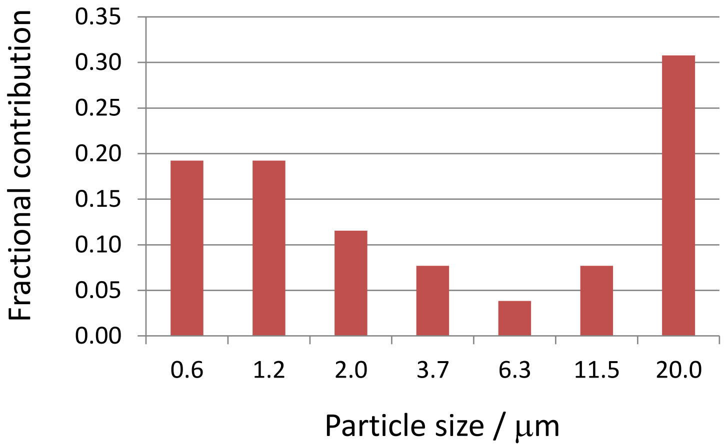

**Figure S31.** Fractional contributions of the different particle sizes to construct the composite uptake profiles.

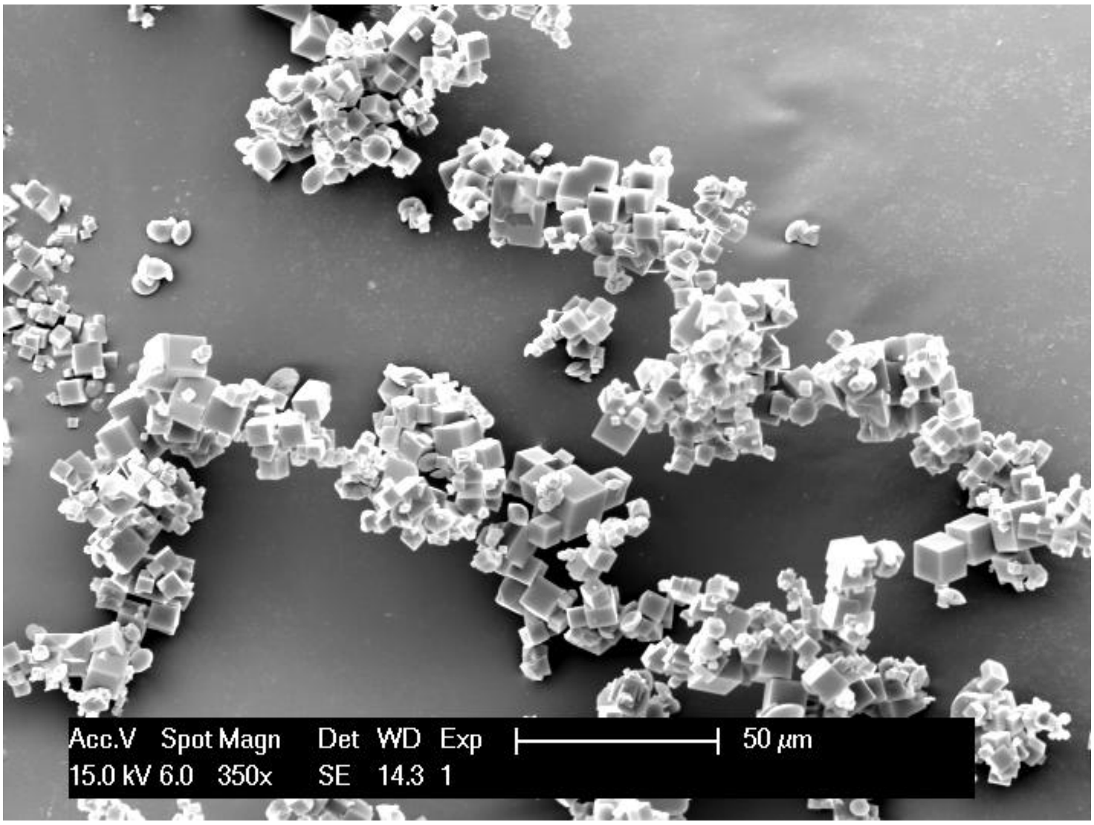

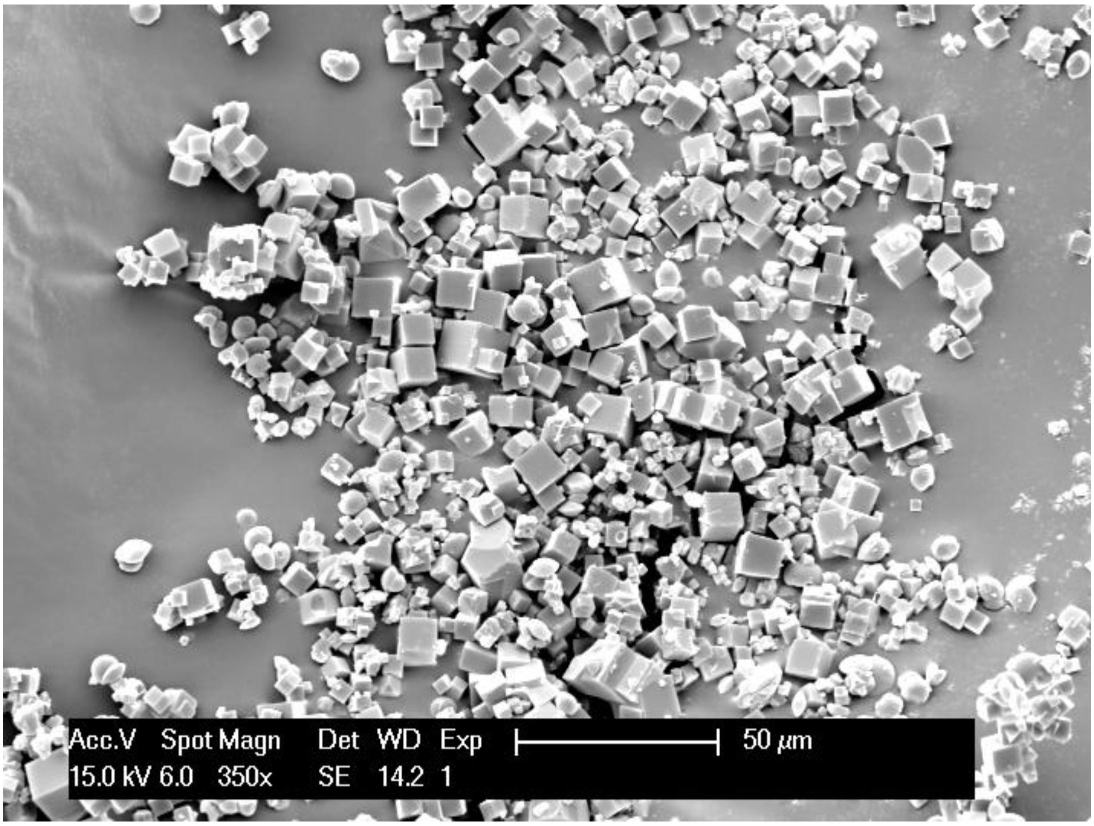

**Figure S32.** SEM pictures of the MFU-4 sample used in the uptake measurements.

The fractional contribution of each profile was kept the same for all four experiments. The Table S10 indicates the used contributions of the various sizes.

**Table S10**. Collected diffusivity data for the largest particles studied.

| | $T$ | $t_{90}$ | $\tau_{\text{diff}}$ | $D_{app}$ | ratio | $E_{act}$ |
|---|---|---|---|---|---|---|
| | [K] | [s] | [s] | [$m^2$/s] | | [kJ/mol] |
| $N_2$ | 195 | 4700 | 705000 | 1.58 E-17 | 52.2 | 18.5 |
| | 298 | 90 | 13500 | 8.23 E-16 | | |
| $CO_2$ | 195 | 66 | 9900 | 1.12 E-15 | 4.4 | 6.9 |
| | 298 | 15 | 2250 | 4.94 E-15 | | |

Taking the largest particles with an edge of 20 micrometer, their performance corresponds with that of a sphere of that diameter (the same volume to surface area ratio), and the same characteristic diffusion length, so for the largest particles $L = d_p/6 = 3.3*10^{-6}$ m. This size is used to calculate the apparent diffusivities for the two gases at 195 and 298 K. Results are given in the Table S10, and the apparent activation energies as well, with a lower value found for $CO_2$, 6.9 kJ/mol, versus 18.5 kJ/mol for $N_2$.

Concluding from these results:

- Uptake profiles confirm the slower diffusion of nitrogen compared with carbon dioxide.
- Diffusivities are small: ~ $10^{-15}$ for $CO_2$ and $10^{-16}$-$10^{-17}$ $m^2/s$ for $N_2$.
- Apparent activation energies 7 and 18 kJ/mol for $CO_2$ and $N_2$, respectively, in qualitative agreement with the calculated values 9 and 34 kJ/mol for $CO_2$ and $N_2$, respectively.